INTERNATIONAL JOURNAL OF PHARMACEUTICAL SCIENCES
[ISSN: 0975-4725; CODEN(USA): IJPS00]
Journal Homepage: https://www.ijpsjournal.com

OPEN ACCESS

Review Article

Oroxylin A-Loaded Zwitterionic Mesoporous Silica Nanoparticles: A Promising Platform for Targeted Lung Cancer Therapy

Mehetre Rutuja*, Dr. Sachin Aglave, Dr. Vijay Jadhav, Dr. Nitin Jain, Dr. Usha Jain

Rastrasanth College of Pharmacy, Kokamthan, Kopergaon

ARTICLE INFO

Published: 02 July 2026
Keywords:
Lung cancer; Oroxylin A; Mesoporous silica nanoparticles; Zwitterionic functionalization; Sulfobetaine; Nanomedicine; Targeted drug delivery; Protein corona inhibition; Tumor targeting; Anticancer therapy; A549 cells; Controlled drug release; Nanotherapeutics; Precision oncology; Drug delivery systems
DOI:
10.5281/zenodo.21154768

ABSTRACT

Lung cancer remains the leading cause of cancer-related mortality worldwide, with therapeutic outcomes often constrained by poor drug selectivity, systemic toxicity, multi drug resistance, and limited intracellular drug accumulation. Nanotechnology-based drug delivery systems have emerged as promising strategies to overcome these limitations and improve therapeutic efficacy. Among various nanocarriers, mesoporous silica nanoparticles (MSNs) have attracted considerable attention owing to their high surface area, tunable pore architecture, excellent biocompatibility, and versatile surface chemistry that enable efficient loading and controlled release of anticancer agents. Recent advances in surface engineering have highlighted the potential of zwitterionic functionalization to impart superior antifouling characteristics, minimize protein corona formation, prolong systemic circulation, and enhance tumor accumulation through improved stealth behavior. Oroxylin A, a naturally occurring flavonoid with significant anticancer activity, has demonstrated promising therapeutic effects against lung cancer; however, its clinical application is limited by poor aqueous solubility and inadequate cellular uptake. The integration of Oroxylin A with zwitterion-functionalized MSNs represents a novel strategy to improve drug bioavailability, intracellular delivery, and cytotoxic efficacy against lung cancer cells. This review comprehensively discusses the pathophysiology of lung cancer, current therapeutic limitations, the principles of nanoparticle-mediated drug delivery, the structural and functional attributes of MSNs, and the biological advantages conferred by zwitterionic surface modification. Furthermore, recent advances in targeted, stimuli-responsive, and theranostic silica-based nanoplatforms are critically evaluated with emphasis on their translational potential for precision oncology. The emerging evidence suggests that zwitterionic MSN systems constitute a promising platform for the development of next-generation nanotherapeutics for effective and targeted lung cancer management.

***Corresponding Author:** Mehetre Rutuja
Address: *Rastrasanth College of Pharmacy, Kokamthan, Kopergaon.*
Email ✉: rutujamehetre09@gmail.com

Relevant conflicts of interest/financial disclosures: The authors declare that the research was conducted in the absence of any commercial or financial relationships that could be construed as a potential conflict of interest.

INTRODUCTION

1.1.Global Burden of Lung Cancer

Lung cancer remains one of the most clinically challenging malignancies of the 21st century, consistently ranking as the leading cause of cancer-related mortality across both developed and developing nations. According to the Global Cancer Statistics compiled by the International Agency for Research on Cancer, lung cancer accounts for approximately 2.2 million new cases annually and is responsible for nearly 1.8 million deaths each year, representing close to 18% of all cancer deaths globally. This alarming epidemiological burden places lung cancer ahead of colorectal, breast, and prostate cancers in terms of mortality, underscoring the urgent need for improved diagnostic and therapeutic strategies. The incidence is particularly high in regions with substantial tobacco consumption, occupational exposure to carcinogens such as asbestos and silica dust, and high levels of air pollution including particulate matter (PM2.5) and indoor biomass smoke—factors of escalating relevance in rapidly industrializing nations including India, China, and Southeast Asian countries.

In the Indian context, lung cancer represents a growing public health crisis. India accounts for a significant proportion of the global lung cancer burden, with incidence rates rising steadily over the past two decades. According to the Indian Council of Medical Research and National Cancer Registry Programme data, lung cancer is among the top five most common cancers in Indian males, and its prevalence among females is also increasing due to indoor air pollution from chulha cooking, passive smoking exposure, and biomass fuel combustion. Urban centers such as Mumbai, Delhi, Chennai, Kolkata, and Pune report significantly higher incidence rates compared to rural regions, largely attributable to vehicular emissions, industrial pollution, occupational exposure, and changing lifestyle patterns. The median age at diagnosis in India tends to be lower than in Western countries, with many patients presenting in their fourth and fifth decades of life, indicating a potentially more aggressive disease course in the genetically and environmentally primed Indian population.

1.2 Clinical Gaps Necessitating Nanomedicine

Late-stage presentation remains a major challenge, with a large majority of Indian patients diagnosed at advanced stages (III/IV) when curative surgical options are limited, resulting in a five-year survival rate of less than 20% in most Indian cohorts. The socioeconomic impact is profound: lung cancer disproportionately affects low- and middle-income populations with limited access to screening programs, specialized oncology care, and expensive targeted therapies. The absence of organized lung cancer screening programs comparable to those in the United States or European Union means that most cases in India are detected incidentally or symptomatically at advanced stages. Efforts to integrate low-dose computed tomography screening into the national health framework are still in early stages, and awareness about risk factors and early warning signs remains inadequate in the general population.

This multifactorial mortality profile defines the rationale for therapeutic innovation through nanomedicine, particularly nanoparticle-based drug delivery systems capable of selective tumor targeting, controlled drug release, and circumvention of biological barriers including protein corona formation, mononuclear phagocyte system clearance, and multidrug efflux.

1.3 The Convergence of Nanomedicine and Natural Product Oncology

Among diverse nanoparticle platforms explored for oncological applications, mesoporous silica nanoparticles occupy a uniquely advantageous position owing to their extraordinarily high surface area (700–1200 m^2/g), tunable mesopore diameter, large pore volume, thermal and chemical stability, and well-characterized surface silanol chemistry that facilitates diverse functionalization strategies. Their proven ability to load and retain hydrophobic drug molecules within their mesopore channels makes them particularly suited for compounds such as Oroxylin A, a flavonoid with poor aqueous solubility and low cellular uptake. However, unmodified MSNs suffer from rapid protein corona formation upon entering the bloodstream, which triggers opsonization and accelerated clearance by the mononuclear phagocyte system, severely curtailing tumor accumulation.

To address this limitation, zwitterionic functionalization using sulfobetaine or carboxybetaine silane derivatives is incorporated in the present platform. Zwitterionic coatings generate a tightly bound electrostatically induced hydration layer that resists nonspecific protein adsorption far more effectively than conventional PEG coatings, conferring stealth properties, prolonging systemic circulation, and enhancing passive tumor accumulation through the EPR effect, without triggering anti-coating antibody formation upon repeated dosing he present review integrates these research threads into a coherent analysis of zwitterionic-MSN-mediated Oroxylin A delivery for lung cancer therapy, while contextualizing it within the broader translational nanomedicine landscape.

1.4 Lung Cancer: Epidemiology, Histopathology, and Clinical Challenges

1.4.1 Global and Indian Epidemiology

Lung cancer represents a growing public health crisis globally, with GLOBOCAN statistics highlighting 2.2 million new cases and 1.8 million deaths annually, accounting for close to 18% of all cancer-related deaths worldwide. This positions lung cancer as the single deadliest malignancy, ahead of breast, colorectal, and prostate cancers. In India specifically, the ICMR-NCRP has documented that lung cancer constitutes one of the leading malignancies in males, with rising incidence among females driven by indoor biomass combustion exposure and passive smoking. The Indian demographic burden is compounded by absence of population-wide screening, late presentation, and limited access to advanced therapeutics.

Several well-defined risk factors contribute to lung cancer pathogenesis. Cigarette smoking remains the single largest preventable cause, with tobacco smoke containing over 60 known carcinogens including polycyclic aromatic hydrocarbons (benzo[a]pyrene), nitrosamines, aromatic amines, and benzene derivatives that induce mutagenic DNA damage. Occupational exposures to asbestos, radon, silica dust, diesel exhaust, and certain metals (chromium, nickel, arsenic) increase risk independently and synergistically with smoking. Air pollution, both ambient (PM2.5) and indoor (cooking fumes, second-hand smoke), accounts for an estimated 15–20% of lung cancer cases globally. Genetic predisposition accounts for a smaller but significant fraction of cases, particularly in never-smokers harboring EGFR mutations or ALK rearrangements.

1.4.2 Histological Classification

Lung cancer is classified into two major histological categories based on cell type of origin and biological behavior. Non-small cell lung cancer constitutes approximately 85% of all lung

cancer diagnoses and includes three major subtypes.

Adenocarcinoma is the most common subtype, accounting for nearly 40% of all lung cancers. It predominantly arises in peripheral lung regions, is more commonly seen in non-smokers and women, and is strongly associated with EGFR mutations (exon 19 deletions, L858R), ALK rearrangements, ROS1 fusions, and KRAS G12C mutations—making it particularly amenable to targeted molecular therapies.

Squamous cell carcinoma is the second most common subtype, arising centrally near the bronchi. It is more strongly associated with cigarette smoking history and frequently harbors alterations in FGFR1, DDR2, PIK3CA, and PTEN.

Large cell carcinoma represents a diagnosis of exclusion characterized by undifferentiated cells lacking defining features of adenocarcinoma or squamous cell carcinoma, growing and spreading rapidly with poor prognosis.

Small cell lung cancer, accounting for ~15% of lung cancers, is a highly aggressive neuroendocrine tumor almost exclusively associated with heavy cigarette smoking. SCLC is characterized by rapid doubling times (as short as 30 days), early widespread metastasis, and initial chemosensitivity followed by almost inevitable relapse with resistant disease. Unlike NSCLC, SCLC has limited targetable molecular alterations, and treatment options have remained relatively unchanged for decades (platinum-etoposide remains standard). The classification into NSCLC and SCLC has profound implications for treatment selection, clinical trial design, nanoparticle targeting strategies, and prognosis.

1.4.3 Molecular Pathogenesis

The molecular pathogenesis is a complex multi-step process involving sequential accumulation of genetic and epigenetic alterations. KRAS mutations (predominantly at codon 12, G12C, G12D, G12V) are found in 25–30% of NSCLC cases in smokers, resulting in constitutive activation of RAS/MAPK and PI3K/AKT/mTOR signaling cascades driving uncontrolled proliferation. TP53 mutations occur in over 50% of lung cancers, impairing DNA damage response and apoptotic machinery. STK11/LKB1 mutations co-occur with KRAS in a significant subset of cases.

In non-smokers and younger patients, driver mutations more commonly occur in EGFR (10–15% Western NSCLC, 40–50% Asian NSCLC—particularly adenocarcinomas), ALK, ROS1, RET, MET, BRAF, and NTRK. EGFR mutations, particularly exon 19 deletions and L858R point mutations in exon 21, result in ligand-independent receptor activation and downstream proliferative signaling. The discovery of EGFR mutations and subsequent development of EGFR tyrosine kinase inhibitors (gefitinib, erlotinib, afatinib, osimertinib) represented a paradigm shift in advanced NSCLC therapy. Igenetic alterations including DNA methylation (CDKN2A, RASSF1A, DAPK1 promoter hypermethylation), histone modification (H3K27me3, acetylation), and non-coding RNA dysregulation (miR-21, miR-155, let-7 family) play critical roles in lung carcinogenesis. MicroRNA expression profiles are being explored as diagnostic biomarkers (miR-21 in sputum), prognostic indicators, and therapeutic targets (miRNA mimics and antimiRs in clinical development).

1.4.4.Tumor Microenvironment

The tumor microenvironment represents the complex ecosystem surrounding cancer cells, comprising stromal fibroblasts, endothelial cells,

immune cells, ECM components, and soluble mediators (cytokines, chemokines, growth factors). The TME actively participates in tumor initiation, progression, immune evasion, and resistance to therapy.

lung cancer, the TME is highly immunosuppressive. Tumor-associated macrophages, predominantly M2-phenotype, secrete immunosuppressive cytokines IL-10 and TGF-β that inhibit cytotoxic T lymphocyte activity and promote tumor angiogenesis and invasion. Myeloid-derived suppressor cells further dampen anti-tumor immune responses via reactive oxygen species production and T cell proliferation suppression. Regulatory T cells accumulate within tumors and suppress effector immune cell function through IL-10 and CTLA-4-mediated mechanisms. The immunosuppressive milieu contributes to the limited efficacy of immunotherapy in approximately 70% of NSCLC patients who derive no long-term benefit from checkpoint inhibition.

Cancer-associated fibroblasts represent another major stromal component that remodels ECM through secretion of collagen, fibronectin, and matrix metalloproteinases (MMP-2, MMP-9), creating a dense physical barrier impeding drug penetration into the tumor core. CAFs also secrete HGF and FGF that activate pro-survival signaling. Elevated interstitial fluid pressure within solid tumors, a consequence of abnormal vasculature and dense ECM, creates a pressure gradient opposing convective drug delivery.

Tumor vasculature in lung cancer is structurally and functionally abnormal: tortuous, leaky blood vessels with irregular blood flow create hypoxic regions and acidosis. Aberrant vasculature with widened interendothelial junctions (200–2000 nm gaps), driven by VEGF overexpression, bradykinin, and nitric oxide, creates size-dependent selective permeability exploited by EPR-mediated nanoparticle accumulation The acidic TME (extracellular pH 6.5–7.0, endolysosomal pH 5.0–5.5) has been exploited for pH-responsive drug release systems, directly relevant to mesoporous silica nanoparticle design.

1.4.5. Treatment Modalities

Surgery remains the cornerstone of curative-intent treatment for early-stage NSCLC (stages I and II). Procedures range from wedge resection and segmentectomy for small peripheral tumors to lobectomy and pneumonectomy for larger or centrally located lesions. Video-assisted thoracoscopic surgery and robotic-assisted thoracic surgery have largely replaced open thoracotomy, offering reduced morbidity, shorter hospital stays, and equivalent oncological outcomes. Only approximately 20–25% of NSCLC patients present with resectable disease at diagnosis, severely limiting surgery's curative applicability.

Platinum-based doublet chemotherapy (cisplatin/carboplatin + paclitaxel, gemcitabine, pemetrexed, or vinorelbine) has long served as backbone treatment for advanced NSCLC. While chemotherapy improves survival and quality of life versus best supportive care, benefits are modest (median OS improvement 2–4 months) and come at the cost of significant systemic toxicity including myelosuppression, nephrotoxicity (cisplatin), neurotoxicity, ototoxicity, and gastrointestinal adverse effects. Resistance, both intrinsic and acquired, remains a major obstacle.

Targeted therapy has been transformed by identification of oncogenic driver mutations. EGFR TKIs (gefitinib, erlotinib, afatinib, osimertinib), ALK inhibitors (crizotinib, alectinib, brigatinib, lorlatinib), and inhibitors targeting

ROS1, BRAF V600E, RET, MET exon 14, and KRAS G12C (sotorasib, adagrasib) achieve high response rates and prolonged progression-free survival in biomarker-selected populations. Howevr, resistance inevitably develops through diverse mechanisms including secondary target mutations (T790M in ~50–60% of acquired EGFR TKI resistance, C797S as next-generation mutation), bypass pathway activation (MET amplification, HER2 amplification), histologic transformation (NSCLC to SCLC transformation in ~5–10%), and drug efflux.

Immunotherapy with immune checkpoint inhibitors targeting PD-1/PD-L1 axis—pembrolizumab, nivolumab, atezolizumab, durvalumab—has emerged as a major therapeutic advance. These agents demonstrate durable responses and improved overall survival as monotherapy or combined with chemotherapy. However, only a subset of patients (20–30%) derive meaningful long-term benefit, and predictive biomarkers beyond PD-L1 expression (tumor mutational burden, tumor-infiltrating lymphocytes, gene expression signatures) remain incompletely characterized. Immune-related adverse events (irAEs) can affect virtually any organ system—colitis, hepatitis, pneumonitis, thyroiditis, hypophysitis, myocarditis—ranging from manageable to life-threatening.

1.4.6.Unmet Clinical Needs

Despite advances, advanced lung cancer prognosis remains poor. Severa limitations underscore the urgent need for novel delivery strategies:

1. **Poor tumor selectivity** of conventional chemotherapy results in widespread systemic toxicity that limits safely administered doses and therapeutic efficacy at tumor sites, with non-selective distribution exposing healthy tissues.
2. **Drug resistance** develops through multiple mechanisms: drug efflux pump upregulation (P-glycoprotein/MDR1, MRP1, BCRP), metabolic inactivation, target alterations, enhanced DNA damage repair, and apoptotic evasion.
3. **Limited biomarker-defined populations** for targeted therapy restrict applicability of precision oncology, with the bulk of patients lacking actionable mutations.
4. **ICI resistance** affects 70–80% of patients, with primary resistance from lack of pre-existing T cell infiltration ("cold tumors") and acquired resistance through T cell exhaustion, antigen loss, and immunosuppressive TME remodeling.
5. **High cost and limited accessibility** of immunotherapy and targeted agents in resource-constrained settings such as India further widen the global equity gap in lung cancer care.

These collective limitations highlight the compelling rationale for nanoparticle-based drug delivery systems capable of selective tumor targeting, minimization of systemic toxicity, overcoming drug resistance, and enabling combination with existing therapies for synergistic effects.

2. NANOPARTICLE-BASED DRUG DELIVERY IN CANCER THERAPY

2.1 Fundamentals of Nanomedicine

Nanomedicine represents the application of nanotechnology principles to disease prevention, diagnosis, and treatment, utilizing materials and devices at the nanoscale (1–1000 nm range). Materials at this scale possess unique properties distinct from bulk counterparts: exceptionally high

surface area-to-volume ratios, quantum mechanical effects, enhanced reactivity, and tunable optical, magnetic, and electronic characteristics. In cancer therapy, nanomedicine enables precise spatial and temporal control over drug release, improved pharmacokinetic profiles, reduced systemic toxicity, tumor-selective drug accumulation, and theranostic integration.

2.2 Classification of Nanoparticles

Nanoparticle systems for drug delivery are broadly classified by composition into:

Organic nanoparticles include liposomes, polymeric nanoparticles, solid lipid nanoparticles, nanoemulsions, dendrimers, cyclodextrin-based nanoparticles, and protein-based nanoparticles (albumin-bound paclitaxel/Abraxane, FDA-approved 2005). Liposomes carry both hydrophilic drugs in their aqueous interior and hydrophobic drugs in lipid bilayers but suffer physical instability and opsonization-induced rapid clearance.

Inorganic nanoparticles include gold nanoparticles, iron oxide nanoparticles, carbon nanotubes, quantum dots, and silica nanoparticles. Mesoporous silica nanoparticles stand distinct from other inorganic systems through their exceptionally high surface area (700–1200 m^2/g), large pore volume, tunable pore size, and versatile silica surface chemistry enabling diverse functionalization strategies.

Hybrid nanoparticles combine organic and inorganic components for synergistic properties, e.g., lipid-coated PLGA-PEG-hybrid systems, lipid-coated silica, polymer-metal organic framework composites.

2.3 Passive and Active Targeting

Two principal targeting strategies underpin nanomedicine:

Passive targeting through the EPR effect exploits the aberrant, leaky vasculature and defective lymphatic drainage of solid tumors, enabling preferential accumulation of nanoparticles in the 10–200 nm size range. The Effect was first described by Maeda and Matsumura in 1986 and has since become the foundational concept for anticancer nanomedicine design. In normal vasculature, tight endothelial junctions restrict macromolecular passage. In tumor vasculature, characterized by widened interendothelial junctions (200–2000 nm gaps), irregular pericyte coverage, and overexpression of vascular permeability factors, preferential accumulation of appropriately sized nanoparticles occurs. Defective lymphatic drainage prevents clearance, prolonging intra-tumor retention.

Active targeting supplements passive accumulation through surface decoration with recognition moieties (monoclonal antibodies, antibody fragments, peptides, aptamers, small molecules) binding receptors overexpressed on cancer cells: folate receptor alpha in ~30–40% of NSCLC, EGFR in 40–80%, transferrin receptor in highly proliferative cells, HER2, integrin $\alpha v\beta 3$ in tumor vasculature, CD44 in cancer stem cells. Active targeting primarily enhances intracellular delivery through receptor-mediated endocytosis rather than altering extravasation.

2.4 EPR Effect in Lung Cancer

In lung cancer, EPR-mediated accumulation is complicated by tumor heterogeneity, elevated interstitial fluid pressure, the dense stromal compartment in certain histological subtypes, and unique pulmonary circulation dynamics. Nanoparticle administered intravenously must survive first-pass through pulmonary capillaries

before reaching systemic circulation, with significant sequestration possible depending on size, charge, and surface properties. Strategies to enhance EPR effect include tumor vasculature normalization (bevacizumab), mild hyperthermia (39–42°C for 30–60 min before nanoparticle administration), and pharmaceutical modulation of vascular permeability. Zwitterionic functionalization directly enhances EPR-based targeting by providing resistance to plasma protein adsorption and macrophage phagocytosis, thereby prolonging systemic circulation and increasing the probability of tumor accumulation across multiple vascular passages.

2.5 Comparave Nanoparticle Analysis

A comparative understanding of polymeric, lipidic, and inorganic nanoparticle systems provides essential context for appreciating the unique advantages of mesoporous silica nanoparticles.

Polymeric nanoparticles fabricated from PLGA, PLA, PCL, and chitosan offer sustained release through polymer matrix degradation, excellent encapsulation efficiency, and ability to incorporate targeting ligands. However, they suffer from batch-to-batch variability, relatively low drug loading capacity (~5–15%), and potential toxicity of accumulated polymer degradation products.

Liposomes are clinically most advanced, with Doxil and Abraxane benchmarks. However, liposomal systems suffer from physical instability during storage, drug leakage, opsonization-induced rapid clearance, and limited loading capacity for hydrophobic drugs unless incorporated into the bilayer.

Gold nanoparticles offer photothermal therapy potential but raise concerns regarding long-term biodistribution, hepatic/splenic accumulation, and clearance.

Iron oxide nanoparticles find application as MRI contrast agents and in magnetic hyperthermia but have limited drug loading capacity (~1–5%).

Mesoporous silica nanoparticles stand apart through their exceptionally high surface area (700–1200 m^2/g), tunable pore diameter (2–10 nm), large pore volume (0.5–2.5 cm^3/g), narrow pore size distribution enabling size-selective loading, and versatile silanol surface chemistry. MSNs can accoodate substantially higher drug loading (20–40% w/w) than other systems, and the silanol chemistry permits covalent modification with amino, carboxyl, thiol, epoxide, and zwitterionic groups through well-established silane chemistry.

3. BIOLOGICAL BARRIERS TO NANOPARTICLE DELIVERY AND PROTEIN CORONA

3.1 Systemic Circulation Barriers

The first barrier encountered by intravenously administered nanoparticles is blood itself. Plasma proteins including albumin (most abundant, 35–50 g/L), fibrinogen, immunoglobulins, complement proteins, and apolipoproteins rapidly adsorb onto nanoparticle surfaces forming a protein corona within seconds to minutes of exposure. This protein corona fundamentally alters the biological identity of the nanoparticle, masks surface targeting ligands, alters cellular uptake pathways, and triggers MPS recognition. Rapid MPS-mediated clearance in liver and spleen (splenic macrophages) dramatically reduces the fraction of administered nanoparticles reaching tumors, with estimates suggesting <1% of injected dose typically accumulating at tumor sites even under optimal conditions.

3.2 Protein Cona Formation and Composition

Protein corona formation is a dynamic two-stage process :

Stage 1: Abundant high-affinity proteins rapidly adsorb, forming a tightly associated monolayer with residence times >hours. The hard corona composition directly reflects the thermodynamic equilibrium between protein-nanoparticle affinity and protein-protein displacement dynamics.

Stage 2: Lower-affinity proteins form a more loosely associated secondary layer with rapid exchange kinetics (seconds to minutes).

Corona composition is dictated by surface charge (positive surfaces attract anionic proteins like albumin; negative surfaces selectively adsorb cationic proteins), hydrophobicity (hydrophobic surfaces attract fibrinogen, IgG), curvature (high-curvature small nanoparticles show different corona profile than larger), and functional groups. For positively charged or hydrophobic surfaces, corona formation is pronounced, leading to rapid opsonization.

The corona dictates biological fate in ways that can be either deleterious or beneficial. **Opsonins** (immunoglobulins, complement C3b, C4b, C-reactive protein) promote phagocytosis by tagging nanoparticles for MPS recognition. **Dysopsonins** (clusterin, apolipoproteins, certain albumin conformations) reduce macrophage uptake and may redirect nanoparticles to alternative biodistribution pathways. Corona-driven uptake may occasionally be useful (e.g., apolipoprotein E binding enables LDL-receptor-mediated uptake across the blood-brain barrier), but generally constitutes a major barrier to selective tumor targeting.

3.3 Zwitterion Coatings Versus PEG

PEGylation has been the conventional gold-standard approach for creating stealth nanoparticles, operating through steric repulsion against protein adsorption. However, PEG suffrs from critical limitations:

1. **Accelerated blood clearance phenomenon:** Repeated doses of PEGylated nanoparticles trigger anti-PEG IgM/IgG antibody production, dramatically reducing circulation time of subsequent doses—a major limitation for chronic cancer therapy.

2. **Oxidative degradation:** PEG's ether linkages ($–CH_2–CH_2–O–$) are susceptible to oxidative degradation via alcohol dehydrogenase, aldehyde oxidase, and cytochrome P450 enzymes in vivo, compromising long-term stability.

3. **Limited performance in complex media:** PEG performance degrades in high-salt and high-protein conditions.

Zwitterionic functionalization addresses each limitation through a fundamentally different mechanism. The simultaneous present cationic and anionic groups of zwitterions create a strong electric dipole that electrostatically attracts and organizes water molecules into a tightly bound hydration layer. This hydration shell acts as a physical and energetic barrier—proteins approaching the surface must displace bound water, which is thermodynamically costly. Zwitterionic polymer brushes grafted onto planar surfaces and nanoparticles reduce nonspecific protein adsorption from undiluted blood plasma to <0.3 ng/cm², substantially below complement activation thresholds. Critically, zwitterionic coatings do not trigger anti-coating antibody formation upon repeated dosing, providing durable, repeatable stealth functionality suitable for sustained therapeutic regimens.

4. MESOPOROUS SILICA NANOPARTICLES: STRUCTURE, SYNTHESIS, AND SURFACE CHEMISTRY

4.1 Structural Architecture

MSNs possess regular arrangements of cylindrical mesopores (2–50 nm by IUPAC classification) creating enormous internal surface area for drug loading. The principal architectural types include:

MCM-41: Two-dimensional hexagonal arrangement of parallel cylindrical pores, pore size 2–5 nm, high surface area (~1000 m^2/g), high pore volume (~1 cm^3/g). Most extensively studied for drug delivery due to well-characterized hexagonal symmetry.

MCM-48: Three-dimensional cubic bicontinuous pore network, pore size 2–4 nm, surface area ~900 m^2/g, provides improved diffusion/connectivity versus 2D systems.

SBA-15: Larger pore diameters (5–10 nm) with thicker pore walls (3–6 nm) and microporous interconnections, conferring greater hydrothermal and mechanical stability.

MSN surface silanol groups exist as isolated (single Si-OH on one silicon), geminal (two Si-OH on the same silicon), and vicinal (adjacent Si-OH on neighboring silicons connected through hydrogen bonding) forms at density ~4–5 OH/nm^2, providing a total of ~2-5 × 10^{18} silanol groups per gram of MSN for versatile functionalization.

5.2 Sol-Gel Synthesis

MSNs are synthesized through sol-gel condensation of silica precursors in the presence of structure-directing surfactants:

- **CTAB (cationic quaternary ammonium)** for MCM-type materials
- **Pluronic P123 (non-ionic triblock copolymer)** for SBA-type materials
- **F127, Brij surfactants** for alternative architectures

The synthesis proceeds through: surfactant dissolution and self-assembly into micelles above CMC (critical micelle concentration); silica precursor addition undergoing hydrolysis (Si-OR + H_2O → Si-OH + ROH) and condensation (Si-OH + Si-OH → Si-O-Si + H_2O or Si-OH + Si-OR → Si-O-Si + ROH); silica condensation around micellar templates; aging and strengthening of the silica framework; surfactant template removal by calcination (550°C for 5 h) or solvent extraction (HCl/ethanol reflux or NH_4NO_3/ethanol).

Particle size, pore diameter, pore volume, and morphology are controlled by adjusting silica-to-surfactant ratio, reaction temperature, pH, co-solvent addition (ethanol slows hydrolysis), and pore expanders (trimethylbenzene enlarges pore diameter for SBA-type). The Box-Behnken optimization in the present thesis exploits this tunability through systematic variation of CTAB amount (0.25–1.0 g), TEOS volume (5.0–10.0 mL), and reaction temperature (65–90°C).

4.3 Surface Functionalization

Two principal approaches enable surface modification of MSNs:

Post-synthesis grafting: Organosilane reagents react with preformed MSN silanols via hydrolysis/condensation. This offers precise control over functional group density, minimizes mesostructure disruption, and preserves drug-loading capability by permitting drug loading after functionalization. However, uneven distribution can occur with preferential external surface modification.

Co-condensation (one-pot): Simultaneous condensation of TEOS and organosilane during MSN synthesis yields homogeneous organic group distribution throughout the framework but risks mesostructure disruption if organosilane >10–20 mol% and cannot generally be applied after drug loading.

Common functionalizations include amines (APTES, providing $–NH_2$), carboxyls (carboxyethylsilanetriol), thiols, epoxides (3-glycidoxypropyltrimethoxysilane), and zwitterionic groups. The zwitterionic functionalization architecture employed in the present study involves three sequential steps: APTES-mediated amine grafting, deoxycholic acid conjugation via EDC/NHS coupling, and sulfobetaine 12 self-assembly.

5. ZWITTERIONIC MERIALS: CHEMISTRY, CLASSIFICATION, AND BIOLOGICAL RELEVANCE

5.1 Molecular Basis of Zwitterionic Hydration

Zwitterionic materials contain both cationic and anionic functional groups within the same molecular unit with overall electrical neutrality. The coexistence of opposite charges creates a strong electric dipole that interacts powerfully with surrounding water molecules through electrostatic mechanisms. The quaternary ammonium cation ($–N^+(CH_3)_3–$) electrostatically attracts the oxygen atoms of water molecules, while the sulfonate ($–SO_3^-$) or carboxylate ($–COO^-$) anion attracts the hydrogen atoms of water. This dual coordination organizes water molecules into a tightly bound hydration layer with binding energies of 50–100 kJ/mol per water molecule, compared to ~20–30 kJ/mol for PEG-mediated hydrogen bonding hydration. The thermodynamic stability of this hydration layer exceeds that of conventional hydrophilic polymer hydration, providing the molecular foundation for exceptional antifouling.

5.2 Classification Zwitterionic Materials

Three principal zwitterionic families are employed in biomedical applications**:**

Phosphorylcholine-bas zwitterions are naturally occurring zwitterionic head groups found in the outer leaflet of mammalian cell membranes. PC-based polymers, including poly(2-methacryloyloxyethyl phosphorylcholine), mimic cell membrane non-fouling properties with excellent hemocompatibility and low immunogenicity. Applications include coronary stent coatings, contact lenses, and DNA delivery vectors.

Sulfobetaine-based zwitterions contain a quaternary ammonium cation and sulfonate anion in the same molecule, separated by a short alkyl spacer (typically propyl). Poly(sulfobetaine methacrylate) coatings exhibit outstanding antifouling properties with protein adsorption <0.3 ng/cm² from undiluted plasma. 3-(Dimethyl(3-(trimethoxysilylpropyl)ammonio)propane-1-sulfonate), known as zwitterionic silane or DMAPS-Si, enables direct grafting of sulfobetaine groups onto silica surfaces. The antifouling performance of PSBMA remains robust under high salt and elevated temperatures, conditions where PEG performance degrades.

Carboxybetaine-based zwitterions contain a quaternary ammonium cation and a carboxylate anion. The functional carboxyl group can be chemically activated via EDC/NHS coupling for conjugation of targeting ligands, peptides, antibodies, or other functional moieties without compromising zwitterionic character. This unique bifunctionality makes CB particularly attractive for targeted antifouling nanoparticle systems.

The sulfobetaine 12 (SB12: N-dodecyl-N,N-dimethyl-3-ammonio-1-propanesulfonate) used in the present thesis is a small-molecule zwitterionic surfactant containing a long C12 hydrophobic tail and sulfobetaine head group, capable of self-assembly onto hydrophobic deoxycholic acid-modified MSN surfaces forming a stable zwitterionic outer shell.

5.3 Antifouling Mechanism and Quantification

The antifouling mechanism of zwitterionic coatings operates through a fundamentally different molecular mechanism compared to PEG-based steric repulsion. Zwitterionic coatings crate a tightly bound hydration shell through electrostatically induced water dipole alignment, with binding enthalpies of -50 to -80 kJ/mol per zwitterionic repeat unit as determined by surface plasmon resonance, isothermal titration calorimetry, and quartz crystal microbalance with dissipation measurements. Protein adsorption onto a zwitterionic brush-coated surface requires displacement of this bound water, which is thermodynamically unfavorable at $\Delta G > +20$ kJ/mol for typical plasma proteins.

Quantitative antifouling performance: protein adsorption from undiluted human blood plasma has been measured at <0.3 ng/cm² for zwitterionic polymer brushes versus 5–50 ng/cm² for PEG brushes under identical conditions. Bacterial adhesion is reduced by >99% versus bare controls. Fibroblast cell adhesion onto zwitterionic-modified surfaces is reduced by >95% versus bare surfaces.

In vivo, zwitterionic functionalized nanoparticles demonstrate extended blood circulation half-lives ($t_{1/2}$ often >24 h versus 3–6 h for unmodified MSNs), reduced hepatic/splenic accumulation, enhanced tumor accumulation through the EPR effect (2–5× enhancement versus unmodified), and lack of anti-zwitterion antibody formation upon repeated dosing.

6. OROXYLIN A: PHARMACOGICAL PROFILE AND THERAPEUTIC POTENTIAL

6.1 Natural Origin, Chemistry, and Physicochemical Properties

Oroxylin A (5,7-dihydroxy-6-methoxyflavone; CAS Registry Number 480-11-5; Molecular Formula $C_{16}H_{12}O_5$; Molecular Weight 284.26 g/mol) is a bioactive flavonoid isolated from the roots and stem bark of *Oroxylum indicum* and *Scutellaria baicalensis* (Chinese skullcap/Baikal skullcap). The compound exists as a pale yellow to yellowish crystalline powder, odorless, freely soluble in methanol, ethanol, DMSO, and acetone, sparingly soluble in chloroform, and practically insoluble in water (0.073 ± 0.004 mg/mL).

The Oroxylin A molecule contains:

- **5,7-Dihydroxy substitution** providing two acidic phenolic protons with pKa ~6.5–7.0, contributing to the weak acidic character of the compound.
- **6-Methoxy substitution** modifying electronic distribution and conferring distinct biological activity relative to baicalein.
- **Aromatic A ring** (5,7-dihydroxy, 6-methoxy substituted benzene) and **B ring** (unsubstituted phenyl, providing hydrophobic character).
- **C2-C3 double bond** with C4 carbonyl, characteristic of flavone (versus flavanone) class.
- **Benzopyran-4-one (chromen-4-one) core** with conjugated system enabling UV

absorption at 273 and 321 nm and yellow coloration.

The compound's BCS Class II classification (low solubility, high permeability) underscores the biopharmaceutical challenge that necessitates a rationally engineered nanocarrier system capable of protecting Oroxylin A from premature degradation, improving its solubilization, and directing it selectively toward lung tumor tissue.

6.2 Anticancer Pharmacological Activities

Oroxylin A demonstrates multimodal anticancer activity through multiple mechanistic pathways**:**

G2/M phase cell cycle arrest: Oroxylin A induces G2/M arrest in cancer cells through upregulation of p21 WAF1/CIP1 and p27 KIP1 CDK inhibitors, downregulation of cyclin B1 and Cdc2, and activation of ATM/ATR DNA damage response pathways.

Apoptosis induction: Oroxylin A activates both intrinsic (mitochondrial) and extrinsic (death receptor) apoptotic pathways. Intrinsic pathway activation involves downregulation of Bcl-2 and Bcl-xL, upregulation of Bax and Bak, mitochondrial membrane potential loss, cytochrome c release, caspase-9 and caspase-3 activation. Extrinsic pathway involves FasL upregulation and caspase-8 activation.

PI3K/AKT/mTOR pathway suppression: Oroxylin A inhibits AKT phosphorylation at Ser473, suppressing downstream mTORC1 activation, reducing phosphorylation of S6K1 and 4E-BP1, and inhibiting oncogenic cap-dependent translation. This suppresses tumor growth, survival, and proliferation signals.

NF-κB pathway inhibition: Oroxylin A prevents IκBα phosphorylation and degradation, retaining NF-κB in the cytoplasm and preventing its nuclear translocation and anti-apoptotic gene transcription. This sensitizes cancer cells to apoptotic stimuli.

Warburg effect suppression: Oroxylin A inhibits aerobic glycolysis in cancer cells through downregulation of GLUT1, HK2, PKM2, and LDHA, redirecting energy metabolism away from glycolysis and reducing lactate production, with potential normalization of tumor microenvironment pH.

MDM2 downregulation and p53 activation: Oroxylin A disrupts the MDM2-p53 negative feedback loop by downregulating MDM2 expression, leading to p53 stabilization, nuclear accumulation, and activation of p53 target genes for cell cycle arrest and apoptosis.

Tumor invasion and metastasis suppression: Oroxylin A inhibits MMP-2 and MMP-9 expression and enzymatic activity through suppression of NF-κB-mediated transcriptional activation, reducing ECM degradation and metastatic potential. Inhibition of EMT transcription factors further reduces metastatic capacity.

6.3 Pharmacokinetics and Biopharmaceutical Challenges

Despite this compelling pharmacological profile, clinical translation of Oroxylin A is severely hampered by fundamental biopharmaceutical limitations**:**

1. **Poor aqueous solubility** (0.073 mg/mL in water, 0.087 mg/mL in pH 7.4 buffer) limits dissolution rate and oral bioavailability.

2. **Rapid hepatic metabolism:** Phase II biotransformation via glucuronidation (UGT1A1, UGT1A9) and sulfation (SULT1A1, SULT1A3), with first-pass

metabolism reducing systemic exposure after oral administration.

3. **Short plasma half-life** (~2–4 h) necessitates frequent dosing, reducing patient compliance and therapeutic efficacy.

4. **Low and variable oral bioavailability** (<30% across species).

5. **Non-selective biodistribution** with accumulation in healthy tissues causing off-target effects.

6. **P-glycoprotein efflux** contributing to multidrug resistance and reducing intracellular drug accumulation.

These interrelated limitations collectively establish the rationale for the zwitterionic MSN delivery platform developed in the present thesis, providing solubilization (mesopore loading transforms crystalline Oroxylin A into amorphous form), protection, passive targeting (zwitterionic stealth functionality prolongs circulation), and enhanced cellular uptake (zwitterionic dipole-mediated interactions increase endocytosis).

7. RATIONALE FOR ZWITTERIONIC-MSN DELIVERY SYSTEM

The integration of mesoporous silica nanoparticles and zwitterionic coatings in the Oroxylin A delivery platform addresses multiple interdependent therapeutic challenges**:**

1. **Drug solubilization:** Mesopore loading transforms crystalline Oroxylin A into a more readily soluble amorphous state within the confined pore geometry, addressing the 0.073 mg/mL aqueous solubility limitation.

2. **Protection from degradation:** MSN encapsulation shields Oroxylin A from premature hepatic metabolism (glucuronidation, sulfation) and from environmental degradation (oxidation, hydrolysis) during systemic circulation, extending biological half-life.

3. **Passive tumor targeting:** Zwitterionic stealth functionality resists protein corona formation, prolonging systemic circulation (EPR probability per vascular pass is 0.01–0.1%) and amplifying tumor accumulation across many vascular passages.

4. **Enhanced cellular uptake:** Zwitterionic dipole-mediated interactions with cancer cell membrane lipid head groups facilitate membrane association and endocytic uptake, surpassing both PEG-coated and unmodified MSN uptake rates.

5. **Sustained release:** Mesopore sequestration enables controlled biphasic release with diffusion and erosion mechanisms maintaining therapeutic drug concentrations over 12+ hours.

The design strategy employs a three-component surface architecture:

- **Deoxycholic acid** hydrophobic inner shell: Provides both drug retention capacity through hydrophobic interactions with the Oroxylin A flavone scaffold, and free carboxyl groups for EDC/NHS-mediated covalent conjugation with the underlying amine-modified surface.

- **APTES-grafted primary amines:** Form covalent siloxane bonds with MSN surface silanols, providing stable anchoring points for subsequent DCA conjugation.

- **Sulfobetaine 12 self-assembled outer shell:** Creates a net-neutral zwitterionic surface with both quaternary ammonium ($–N^{+}(CH_3)_3$) and

sulfonate ($–SO_3^-$) groups within each molecule, generating the electrostatic hydration layer responsible for the antifouling properties.

The selection of SB12 specifically over carboxybetaine alternatives was motivated by: (i) SB12's commercial availability as a long-tail amphiphilic zwitterion providing simple self-assembly on hydrophobic surfaces; (ii) the well-characterized MTT assay performance of SB12-coated systems in cancer models; (iii) the demonstrated precedent of Gao et al. using DC@SB12-modified MSNs for protein drug oral delivery, validating the chemistry for the present application.

8. PREFORMULATION CHARACTERIZATION OF OROXYLIN A

8.1 Organoleptic Properties and Identification

Oroxylin A was visually examined and the observed characteristics were found to be in close agreement with reported literature values. The drug appeared as a yellow crystalline powder, consistent with flavonoid-class chemistry and the conjugated chromophore responsible for characteristic yellow coloration. It was odourless and existed as a solid at room temperature. These organoleptic properties align precisely with reported values, confirming identity and integrity of the procured drug sample, validating its suitability for subsequent preformulation and formulation studies.

Table 1: Organoleptic Properties and Identification of Oroxylin A

Parameter	Reported Value	Observed Value
Appearance	Crystalline powder	Crystalline powder
Colour	Yellow	Yellow
Odour	Odourless	Odourless
Nature	Solid	Solid

8.2 Melting Point and Thermal Behavior

Melting point determination using the open capillary tube method showed 196–198°C, in close agreement with the reported literature value of 195–197°C. This narrow 2°C experimental deviation confirms the identity and high purity of the drug substance. DSC analysis of pure Oroxylin A revealed a sharp endothermic melting peak at 196.8°C, confirming crystalline nature and indicating minimal impurities.

8.3 UV Spectrophotometric Analysis and Calibration

UV scanning in methanol over 200–400 nm revealed dual absorption maxima at 273 nm and 321 nm, attributed to $\pi \rightarrow \pi^*$ and $n \rightarrow \pi^*$ electronic transitions of the flavone chromophore system. The 273 nm wavelength was selected as the analytical detection wavelength for all subsequent quantitative determinations due to higher sensitivity and minimal interference from potential excipient UV absorption.

A calibration curve constructed at 273 nm over 2–12 µg/mL demonstrated excellent linearity with the regression equation $y = 0.0554x + 0.0033$ and $R^2 = 0.9995$, confirming strict Beer-Lambert compliance.

Table 2: Calibration Curve Data of Oroxylin A in Methanol at 273 nm

Concentration (µg/mL)	Absorbance
2	0.124 ± 0.003
4	0.221 ± 0.005
6	0.334 ± 0.004
8	0.441 ± 0.006
10	0.558 ± 0.007
12	0.671 ± 0.005

Values expressed as mean ± SD (n = 3). The strongly linear calibration curve enables accurate quantification of Oroxylin A in entrapment

efficiency, drug loading, and in vitro drug release studies.

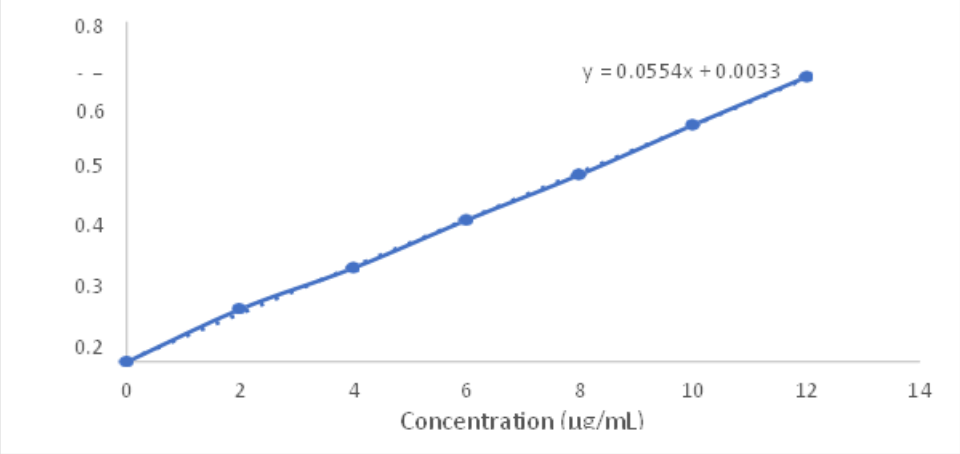

Fig 1: Calibration curve of Oroxylin A in methanol at 273 nm showing linearity across 2–12 µg/mL

8.4 Solubility Assessment

Saturation shake-flask analysis at 25 ± 0.5°C over 24 hours indicated:

Table 3: Solubility of Oroxylin A

Solvent	Observed Solubility (mg/mL)	Classification
Distilled Water	0.073 ± 0.004	Practically Insoluble
Phosphate Buffer pH 7.4	0.087 ± 0.003	Practically Insoluble
Phosphate Buffer pH 6.8	0.069 ± 0.005	Practically Insoluble
Ethanol	8.34 ± 0.21	Slightly Soluble
Methanol	11.62 ± 0.34	Sparingly Soluble
DMSO	61.43 ± 0.87	Freely Soluble
Acetone	4.17 ± 0.18	Slightly Soluble
Chloroform	6.82 ± 0.29	Slightly Soluble

These data confirm Oroxylin A is BCS Class II (low solubility, high permeability) and rationalize the use of methanol (optimal balance of solubilization and volatility for rotary evaporation loading) as the loading solvent, while underscoring the necessity of nanoparticulate formulation.

8.5 FTIR Identification

Fourier transform infrared (FTIR) spectroscopy confirmed the successful synthesis, surface modification, and drug encapsulation within the mesoporous silica nanoparticle system. Pure Oroxylin A exhibited characteristic absorption bands corresponding to phenolic hydroxyl groups, flavone carbonyl functionality, and aromatic ring vibrations, verifying the structural integrity of the drug molecule. Bare mesoporous silica nanoparticles displayed the characteristic silanol and siloxane stretching vibrations associated with the silica framework.

Fourier transform infrared (FTIR) spectroscopy confirmed the successful synthesis, surface modification, and drug encapsulation within the mesoporous silica nanoparticle system. Pure Oroxylin A exhibited characteristic absorption bands corresponding to phenolic hydroxyl groups, flavone carbonyl functionality, and aromatic ring vibrations, verifying the structural integrity of the drug molecule. Bare mesoporous silica nanoparticles displayed the characteristic silanol

and siloxane stretching vibrations associated with the silica framework.

The FTIR analysis demonstrated the successful fabrication of zwitterionic functionalized mesoporous silica nanoparticles capable of efficiently incorporating Oroxylin A while maintaining the chemical integrity of both the drug and the nanocarrier components.

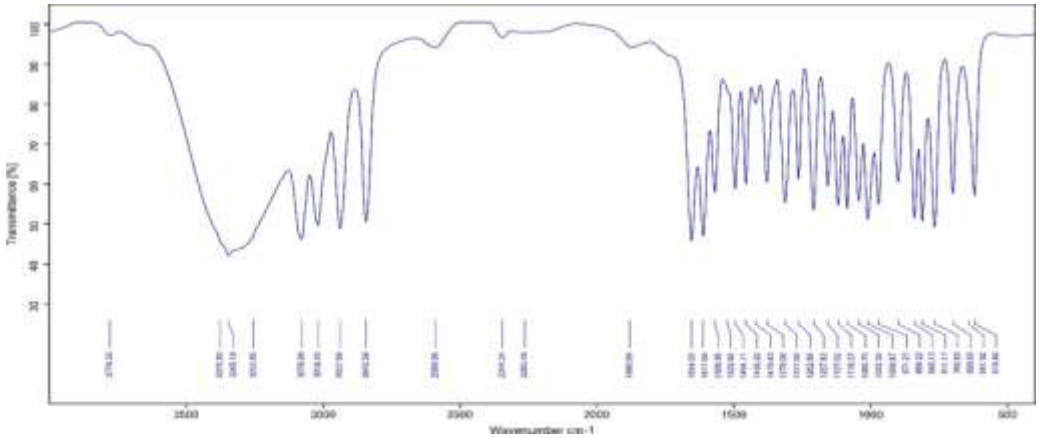

Fig 2: FTIR spectrum of Pure Oroxylin A

9. SYNTHESIS AND SEQUENTIAL FUNCTIONALIZATION PROTOCOL

9.1 MSN Core Synthesis

Bare MSNs were prepared by surfactant-templated sol-gel method. CTAB (0.25–1.00 g, per BBD design) was dissolved in distilled water under stirring, pH adjusted with sodium hydroxide solution (NaOH catalysis ~0.3 M), the mixture heated to 65–90°C (per design), and TEOS (5.0–10.0 mL, per design) added dropwise to initiate hydrolysis and condensation around CTAB micelles. After 4 h reaction, the white precipitate was centrifuged at 10,000 rpm for 10 min, washed thrice with distilled water and ethanol, dried overnight at 80°C, and calcined at 550°C for 5 h in a muffle furnace to remove surfactant, yielding bare MSNs with well-ordered cylindrical mesopores.

9.2 Three-Step Sequent Zwitterionic Functionalization

A sequential three-step post-synthetic surface modification protocol was employed for OXA-loaded MSNs, with each step introduced through precise chemical reactivity:

Step 1: OXA-MSN (100 mg) was dispersed in 40 mL anhydrous ethanol under probe sonication (10 min for homogeneous dispersion), 0.8 mL APTES added dropwise under nitrogen atmosphere to prevent oxidation of the amine, the mixture refluxed at 80°C for 18 h, yielding OXA-MSN-NH_2 via covalent siloxane bond formation between APTES triethoxysilyl groups and MSN surface silanols, releasing ethanol as byproduct. Recovery involved centrifugation at 10,000 rpm for 10 min, washing thrice with anhydrous ethanol to remove unreacted APTES, and vacuum drying at 50°C.

Step 2: OXA-MSN-NH_2 (100 mg was dispersed in 50 mL DMSO, to which 100 mg deoxycholic acid, 50 mg N-hydroxysuccinimide, and 50 mg EDC·HCl (1-ethyl-3-(3-dimethylaminopropyl) carbodiimide hydrochloride) were sequentially added. The mixture reacted at 60°C for 48 h. The EDC/NHS-mediated amide coupling proceeds through: (i) EDC activation of DCA's carboxyl group forming O-acylisourea intermediate; (ii)

NHS displacement forming more stable NHS-ester; (iii) amine nucleophilic attack forming covalent amide bond (–CO-NH–) with EDC/NHS byproduct removal. This yields OXA-MSN-DC with hydrophobic DCA inner coating presenting carboxylate groups available for further functionalization. Recovery involved centrifugation, washing with DMSO then distilled water, overnight drying.

Step 3 (SB12 Zwitterionic Sf-Assembly): OXA-MSN-DC (50 mg) was dispersed in 10 mL distilled water under sonication, a solution of 50 mg SB12 in 5 mL distilled water added dropwise at 500 rpm for 60 min at room temperature, during which SB12 (N-dodecyl-N,N-dimethyl-3-ammonio-1-propanesulfonate) self-assembled onto the DCA-modified surface through hydrophobic C12 tail interactions with DCA steroid rings and electrostatic interactions between SB12 sulfonate and residual surface cationic groups. This generated a net-zero charge zwitterionic outer shell bearing both quaternary ammonium ($–N^+(CH_3)_2–$) and sulfonate ($–SO_3^-$) groups. The final OXA-SB12-MSN was recovered by centrifugation at 12,000 rpm for 10 min, washed thrice with distilled water, lyophilized, and stored at 4°C protected from light.

9.3.. Box-Behnken Design-Dri Formulation Optimization

9.3.1 Methodology Rationale

Three independent variables critical to MSN physicochemical properties were selected based on preliminary screening and literature evidence**:**

- **X_1: CTAB amount (0.25–1.00 g):** Directly governs micelle formation density, pore architecture, particle size. Higher CTAB → denser micelles → smaller particles with larger pore volume.
- **X_2: TEOS volume (5.0–10.0 mL):** Determines silica condensation rate and particle growth extent. Higher TEOS → larger particles with denser silica walls.
- **X_3: Reaction temperature (65–90°C):** Regulates hydrolysis kinetics (rate doubles approximately every 10°C) and condensation rates, affecting both particle size and crystallinity.

A three-factor, three-level Box-Behnken Design using Design Expert® 13 generated 17 experimental runs (5 center points for reproducibility assessment, 8 factorial runs, 4 axial runs) with particle size (Y_1, minimize) and entrapment efficiency (Y_2, maximize) as dependent responses modeled via quadratic polynomial equations.

9.3.2 ANOVA for Particle Size (Y_1)

The quadratic model for particle size demonstrated excellent statistical significance ($F = 76.75$; $p < 0.0001$), indicating the model explained the variance in particle size at >99.99% confidence level. Lack of fit was non-significant $F = 0.9570$, $p = 0.4940$), confirming model adequacy in representing experimental data without systematic deviation. CTAB amount exerted the most dominant linear influence ($F = 434.00$; $p < 0.0001$), followed by TEOS volume ($F = 163.93$; $p < 0.0001$), while reaction temperature alone was non-significant ($F = 0.1515$, $p = 0.7087$). The interaction term BC (TEOS × Temperature) was significant ($p = 0.0367$), indicating non-additive effects of these variables. Quadratic terms A^2 ($p = 0.0405$), B^2 ($p = 0.0003$), and C^2 ($p = 0.0024$) were significant, confirming non-linear response surfaces. Fit statistics indicated excellent model reliability: $R^2 = 0.9900$, adjusted $R^2 = 0.9771$, predicted $R^2 = 0.9238$, with less than 0.2 difference between adjusted and predicted R^2 confirming

strong predictive capability. The adequate precision value of 31.01 indicated strong signal-to-noise ratio.

The regression equation was:

$Y_1 = 163.52 - 50.175A + 30.8375B - 0.9375C + 6.35AB + 5.6AC + 8.775BC + 8.3275A^2 + 22.3025B^2 + 15.3525C^2$

The dominant negative coefficient of A (−50.175) confirmed that increasing CTAB substantially reduces particle size through denser micellar templating, while the positive coefficient of B (+30.8375) confirmed that increasing TEOS progressively increases particle size through enhanced silica condensation and particle growth.

Table 4 : ANOVA for the quadratic model for Particle Size (Y1)

Source	Sum of Squares	df	Mean Square	F-value	p-value	
Model	32056.92	9	3561.88	76.75	< 0.0001	significant
A-CTAB	20140.24	1	20140.24	434.00	< 0.0001	
B-TEOS	7607.61	1	7607.61	163.93	< 0.0001	
C-Reaction Temperature	7.03	1	7.03	0.1515	0.7087	
AB	161.29	1	161.29	3.48	0.1046	
AC	125.44	1	125.44	2.70	0.1442	
BC	308.00	1	308.00	6.64	0.0367	
A^2	291.99	1	291.99	6.29	0.0405	
B^2	2094.32	1	2094.32	45.13	0.0003	
C^2	992.42	1	992.42	21.39	0.0024	
Residual	324.85	7	46.41			
Lack of Fit	135.74	3	45.25	0.9570	0.4940	Not significant
Pure Error	189.11	4	47.28			
Cor Total	32381.76	16				

9.3.3. ANOVA for Entrapment Efficiency (Y_2)

The quadratic model for entrapment efficiency was statistically significant (F = 19.21; p = 0.0004). Lack of fit was non-significant (F = 0.5159, p = 0.6933). CTAB amount (F = 106.37; p < 0.0001) was the most influential variable, while TEOS volume exerted a significant negative influence (F = 28.27; p = 0.0011). The interaction term AB was significant (p = 0.0483), and quadratic terms B^2 (p = 0.0055) and C^2 (p = 0.0250) were significant. $R^2 = 0.9611$ and adjusted $R^2 = 0.9110$ indicated good model fit; adequate precision of 14.41 confirmed a satisfactory signal-to-noise ratio.

The regression equation was:

$Y_2 = 77.14 + 9.2375A - 4.7625B + 0.4C - 3.025AB - 1.15AC - 0.55BC - 2.6325A^2 - 4.8825B^2 - 3.5075C^2$

Higher CTAB levels combined with lower TEOS volumes generated well-ordered mesopore channels with greater surface area, facilitating enhanced drug encapsulation. The negative B coefficient (−4.7625) confirmed that excess TEOS leads to denser silica walls with reduced accessible pore volume.

Table 5 : ANOVA for the quadratic model for Entrapment Efficiency (Y^2)

Source	Sum of Squares	df	Mean Square	F-value	p-value	
Model	1109.36	9	123.26	19.21	0.0004	significant
A-CTAB	682.65	1	682.65	106.37	< 0.0001	
B-TEOS	181.45	1	181.45	28.27	0.0011	
C-Reaction Temperature	1.28	1	1.28	0.1994	0.6687	
AB	36.60	1	36.60	5.70	0.0483	
AC	5.29	1	5.29	0.8243	0.3941	
BC	1.21	1	1.21	0.1885	0.6772	
A^2	29.18	1	29.18	4.55	0.0704	
B^2	100.37	1	100.37	15.64	0.0055	
C^2	51.80	1	51.80	8.07	0.0250	
Residual	44.92	7	6.42			
Lack of Fit	12.53	3	4.18	0.5159	0.6933	Not significant
Pure Error	32.39	4	8.10			
Cor Total	1154.28	16				

Table 6: Fit statistics of Entrapment Efficiency (Y^2)

Std. Dev.	2.53	**R^2**	0.9611
Mean	71.95	**Adjusted R^2**	0.9110
C.V. %	3.52	**Predicted R^2**	0.7824
		Adeq Precision	14.4109

9.3.4.Physicochemical Responses Across Batches

Across the 17 BBD batches:

Table 7: Physicochemical Evaluation Data of Oroxylin A–Zwitterionic Mesoporous Silica Nanoparticle Formulation Batches (RF1–RF17)

	Batch	Particle Size (nm) PDI	Zeta Potential (mV)	% EE	% DL	% Yield
RF1	155.3 ± 4.8	0.212 ± 0.018	−18.2 ± 1.4	73.8 ± 1.8	19.6 ± 0.9	81.4 ± 1.4
RF2	171.4 ± 5.6	0.234 ± 0.021	−19.8 ± 1.7	80.4 ± 2.1	21.2 ± 1.1	85.2 ± 1.6
RF3	218.3 ± 4.6	0.288 ± 0.018	−22.4 ± 1.3	63.4 ± 1.8	17.4 ± 0.8	76.4 ± 1.3
RF4	241.7 ± 5.2	0.314 ± 0.021	−22.8 ± 1.5	65.2 ± 2.1	17.8 ± 0.9	74.8 ± 1.4
RF5	128.6 ± 3.1	0.184 ± 0.011	−16.4 ± 0.9	82.6 ± 1.6	21.5 ± 0.7	85.4 ± 1.0
RF6	112.4 ± 2.7	0.162 ± 0.008	−12.7 ± 1.2	86.4 ± 1.3	22.3 ± 0.6	88.6 ± 0.8
RF7	178.2 ± 3.8	0.256 ± 0.014	−17.8 ± 1.1	71.2 ± 1.5	19.1 ± 0.8	79.2 ± 1.2
RF8	158.4 ± 3.4	0.231 ± 0.013	−15.3 ± 0.7	74.8 ± 1.7	19.9 ± 0.6	81.6 ± 1.1
RF9	234.6 ± 5.8	0.328 ± 0.019	−26.4 ± 1.6	61.7 ± 2.3	17.0 ± 1.1	73.8 ± 1.6
RF10	138.3 ± 3.2	0.196 ± 0.012	−14.6 ± 1.0	79.4 ± 1.8	20.8 ± 0.8	84.2 ± 1.0
RF11	163.6 ± 5.2	0.226 ± 0.019	−19.1 ± 1.6	77.3 ± 2.0	20.4 ± 1.0	83.1 ± 1.5
RF12	169.1 ± 6.1	0.231 ± 0.022	−19.6 ± 1.8	79.4 ± 2.3	21.0 ± 1.2	84.3 ± 1.7
RF13	263.2 ± 6.4	0.381 ± 0.024	−31.6 ± 1.8	58.9 ± 2.6	16.3 ± 1.2	72.4 ± 1.7
RF14	182.7 ± 4.1	0.267 ± 0.016	−16.8 ± 1.1	69.8 ± 1.9	18.8 ± 0.9	78.6 ± 1.3
RF15	226.4 ± 5.1	0.318 ± 0.020	−21.4 ± 1.4	63.8 ± 2.0	17.5 ± 0.8	75.2 ± 1.4
RF16	247.3 ± 5.7	0.356 ± 0.022	−28.4 ± 1.7	60.3 ± 2.4	16.6 ± 1.0	73.6 ± 1.5
RF17	158.2 ± 4.4	0.218 ± 0.017	−18.4 ± 1.5	74.8 ± 1.9	19.9 ± 0.9	82.2 ± 1.4

n = 3; SD = Standard Deviation; EE = Entrapment Efficiency; DL = Drug Loading.

Higher CTAB concentrations promoted smaller, more uniform particles through denser micelle templating, while increased TEOS volume led to larger aggregated particles via excessive silica condensation. PDI was narrower in batches with higher CTAB and lower TEOS, indicating improved homogeneity. Zeta potentials were negative across all batches reflecting partial silanol deprotonation (pKa ~6.5–7.0) compensated by SB12 zwitterionic groups. Entrapment efficiency directly correlated with particle size and available mesopore surface area.

9.3.5. Optimization and Validation

Desirability function optimization (Design Expert® 13) identified the optimal formulation at CTAB 1.0 g, TEOS 5.0 mL, and reaction temperature 77.5°C. Predicted particle size was 108.20 nm and entrapment efficiency 86.40%, with overall desirability of 0.9956—indicating excellent proximity to the theoretical optimum. Experimentally obtained values of 112.4 ± 2.7 nm and 86.4 ± 1.3% showed excellent agreement with percentage biases of only 3.88% and 0.00%, respectively, confirming the robustness and predictive accuracy of the quadratic models.

9.4Characterization of the Optimized Formulation

9.4.1 Particle Size, PDI, and Zeta Potential

Dynamic light scattering revealed particle size of 112.4 ± 2.7 nm with PDI of 0.162 ± 0.008, indicating narrow monomodal size distribution suitable for EPR-mediated tumor accumulation and clathrin-mediated endocytic uptake (optimal 60–200 nm range). The PDI <0.2 indicates good monodispersity important for reproducible in vivo behavior and consistent clinical performance. Zeta potential of −12.7 ± 1.2 mV reflects partial silanol deprotonation compensated by neutralization through net-zero charge zwitterionic SB12 groups, ensuring adequate colloidal stabilization under physiological conditions while reducing non-specific electrostatic interactions with healthy cell membranes.

9.4.2 FTIR Confirmation of Sequential Functionalization

Comparative FTIR analysis across pure Oroxylin A, bare MSNs, zwitterionic functionalized MSNs (OXA-SB12-MSN-DC), and drug-loaded MSNs (OXA-SB12-MSN) confirmed the sequential surface transformation**:**

Table 8: FTIR Spectral Interpretation of Pure Oroxylin A, Bare MSNs, Zwitterionic Functionalized MSNs, and Drug-Loaded MSNs

Assignment	Pure Oroxylin A	Bare MSNs	OXA-SB12-MSN-DC	Drug-Loaded OXA-SB12-MSN
O–H stretching (phenolic/silanol)	3779.33, 3375.93	3455.39	3445.51, 3416.14	3503.14, 3436.62
N–H stretching (amine/amide)	3345.19	-	3335.99	3245.29
Aromatic/ aliphatic C–H	3078.09, 3018.43, 2937.68	2872.14	2925.18, 2853.97	3081.99, 3022.86, 2976.53, 2928.65, 2846.80
C=O (flavone/amide I)	1654.02, 1611.50	1672.65	1642.78	1645.33, 1611.95
N–H bending (amide II) / C=C aromatic	1568.98, 1522.60	-	1564.29, 1544.87	1567.57, 1545.79

C–C aromatic ring stretching	1494.71, 1456.20, 1419.43	1473.03	1480.57, 1455.68	1493.17, 1479.27, 1455.94
C–H bending / S=O symmetric	1379.06, 1311.50	1301.21	1377.60, 1300.80	1377.44, 1304.89
C–O–C / S=O asymmetric	1262.86, 1207.83, 1157.02	1136.19	1241.42, 1182.10	1262.34, 1239.86, 1208.96
Si–O–Si asymmetric stretching	1118.37, 1085.75	1079.86	1116.40, 1080.18	1155.78, 1118.20, 1082.74
Si–OH / C–H out-of-plane bending	971.21, 899.22, 840.13	960.20, 845.53, 800.89	1011.12, 873.03, 838.84	1010.09, 972.03, 897.32, 840.12

The emergence of N–H stretching at 3335 cm^{-1} and amide I carbonyl at 1642 cm^{-1} and amide II band at 1544 cm^{-1} in OXA-SB12-MSN-DC confirmed successful APTES grafting and DCA conjugation via EDC/NHS-mediated amide bond formation. S=O stretching vibrations around 1300 and 1182 cm^{-1} confirmed SB12 zwitterionic coating. The drug-loaded OXA-SB12-MSN retaed all functionalization peaks while displaying reappearance of Oroxylin A-specific aromatic C–H stretching at 3081 cm^{-1} and C=O vibration at 1645 cm^{-1}, with notable broadening and intensity attenuation confirming molecular-level encapsulation and drug-carrier interaction.

9.4.3 DSC Thermogram

DSC thermogram of pure Oroxylin A exhibited a sharp endothermic melting peak at 196.8°C confirming crystalline nature and purity. The physical mixture showed retain drug melting transition at 198.2°C and a second event at 312.6°C attributed to the silicate framework thermal decomposition. Confirmation of physicochemical compatibility was evidenced by absence of new thermal events or significant peak shifts indicating no chemical interaction between Oroxylin A and the zwitterionic MSN carrier components.

9.4.4 Drug Loading Metrics

The drug-to-carrier ratio of 1:2 (w/w) optimized during preliminary screening was justified by considerations of mesopore saturation capacity, surface functionalization stability, and colloidal dispersibility. This ratio achieved drug loading of 22.3 ± 0.6% (DL%, calculated as mass of drug in nanoparticles × 100 / total mass of nanoparticles) and entrapment efficiency of 86.4 ± 1.3% (EE%, calculated as mass of drug entrapped × 100 / mass of drug added) in RF6, confirming high-capacity loading of hydrophobic Oroxylin A within the mesopore network.

9.5 In Vitro Drug Release and Kinetic Modeling

9.5.1 Biphasic Release Pattern

Cumulative in vitro drug release studies at pH 7.4 over 12 h using dialysis membrane diffusion method (12,000 Da MWCO, 50 mL PBS, 100 rpm, 37 ± 0.5°C) revealed clear concentration-dependent patterns governed primarily by particle size. All batches exhibited biphasic release:

- **Initial burst phase (0–2 h):** 13.2–21.8% release, attributable to surface-adsorbed drug rapidly diffusing into medium from the outermost pore openings.
- **Sustained phase (2–12 h):** Slow, diffusion-controlled release of drug sequestered within the mesopore network, governed by drug diffusion coefficients, path length through

mesopore channels, and gradual erosion of the zwitterionic surface layer.

RF6 (smallest particle, 112.4 nm) achieved the highest cumulative release of 76.8 ± 1.54% at 12 h, while RF13 (largest particle, 263.2 nm) released only 46.8 ± 0.98%. This clear inverse relationship between particle size and cumulative release reflects the diffusion path length through mesopore channels being shorter for smaller particles.

9.5.2 Kinetic Model Fitting

Drug release data for RF6 fitted five mathematical kinetic models**:**

Table 9: Kinetic Model Fitting

Kinetic Model	R^2	Mechanism Indication
Zero-order	0.9766	Concentration-independent release (ideal for sustained delivery)
First-order	0.9952	Concentration-dependent release from reservoir
Higuchi	0.9805	Fickian diffusion from matrix
Hixson-Crowell	0.9981	Drug release from eroding matrix with surface area decreasing over time
Korsmeyer-Peppas	0.9988	Anomalous diffusion-controlled release

The Korsmeyer-Peppas model provided the best fit with R^2 = 0.9988 and diffusional exponent n = 0.7250. The n value between 0.5 and 1.0 indicates anomalous non-Fickian diffusion transport, suggesting that Oroxylin A release from the zwitterionic MSN is governed by combined diffusion through mesopore channels AND erosion/relaxation of the surface functionalization layer. This dual release mechanism is therapeutically advantageous: initial burst provides rapid therapeutic onset, while sustained release maintains drug concentrations above cytotoxic thresholds over extended periods.

9.5.3 Physicochemical Drivers of Release Behavior

The biphasic release pattern is mechanistically driven by:

1. **Surface-adsorbed drug fraction:** Following rotary evaporation loading, a fraction of Oroxylin A resides at the external MSN surface and outer pore openings, providing initial burst release independent of controlled release mechanisms.

2. **Pore geometry and tortuosity:** Drug molecules must traverse the mesopore channels (typically 2–4 nm diameter, with variable lengths) by diffusion, with smaller particles presenting shorter average diffusion paths.

3. **Functionalization layer barrier properties:** The DCA hydrophobic inner coating and SB12 zwitterionic layer together retard drug diffusion, slowing the sustained release phase. In vitro drug-surface interactions (hydrophobic DCA-Oroxylin A interactions, electrostatic SB12-Oroxylin A interactions) provide additional rate-limiting effects.

4. **Solution thermodynamics:** Oroxylin A solubility in release medium (0.087 mg/mL in PBS pH 7.4) maintains sink conditions, with higher solubility in albumin-containing media further enhancing apparent release rates.

9.6. Accelerated Stability Under ICH Conditions

9.6.1 ICH-Compliant Protocol

The optimized OXA-SB12-MSN formulation was subjected to accelerated stability testing at 40 ± 2°C and 75 ± 5% RH for three months per ICH

Q1A(R2) guidelines. Samples were evaluated at 0, 1, 2, and 3 months for:

- Physical appearance (white to pale yellow free-flowing powder)
- Particle size by DLS
- PDI
- Zeta potential
- Entrapment efficiency
- Cumulative drug release at 12 h

9.6.2 Stability Findings

Across the three-month accelerated study, the formulation maintained excellent physicochemical stability:

Table 10: Stability study Oroxylin A

Parameter	0 Month	1 Month	2 Month	3 Month
Appearance	Yellow free-flowing powder	Yellow free-flowing powder	Yellow free-flowing powder	Yellow free-flowing powder
Particle Size (nm)	112.4 ± 2.7	113.1 ± 2.9	113.8 ± 3.1	114.6 ± 3.2
PDI	0.162 ± 0.008	0.164 ± 0.009	0.167 ± 0.010	0.169 ± 0.011
Zeta Potential (mV)	−12.7 ± 1.2	−12.4 ± 1.3	−12.1 ± 1.4	−11.8 ± 1.4
% EE	86.4 ± 1.3	85.9 ± 1.4	85.4 ± 1.5	84.8 ± 1.6
% CDR at 12 h	76.8 ± 1.54	76.2 ± 1.58	75.6 ± 1.62	74.9 ± 1.68

The marginal variations across all parameters (≤2% particle size increase, ≤1.6% EE decrease, ≤1.9% CDR decrease) confirm excellent physicochemical stability under accelerated storage conditions, validating the formulation's potential for pharmaceutical development with adequate shelf-life. The slow rate of degradation suggests the formulation may also meet long-term stability requirements (25°C/60% RH), though this requires explicit verification at long-term storage conditions per ICH protocols.

9.6.3 Mechanistic Basis for Stability

The exceptional stability derives from the covalent siloxane anchoring of the APTES layer, the stable amide bond of DCA conjugation (amide hydrolysis negligible below 60°C), and the electrostatic/hydrophobic interactions stabilizing SB12 self-assembly. The minimal particle size change suggests absence of Ostwald ripening or aggregation during storage. Stable entrapment efficiency indicates absence of drug desorption or chemical degradation over the storage period.

9.7. In Vitro Cytotoxicity Against A549 Lung Cancer Cells

9.7.1 MTT Assay Methodology

Cytotoxicity was assessed against A549 human lung adenocarcinoma cells using the MTT assay at five concentrations (5, 10, 20, 40, 80 µg/mL) with 48 h treatment. A549 cells were cultured in DMEM supplemented with 10% FBS and 1% penicillin-streptomycin at 37°C in 5% CO_2 humidified atmosphere. Cells were seeded in 96-well plates at 5×10^3 cells/well and incubated 24 h for adherence before treatment. After 48 h exposure, 20 µL MTT (5 mg/mL) was added per well, 4 h incubation generated formazan crystals through mitochondrial dehydrogenase-mediated reduction of yellow MTT tetrazolium, crystals dissolved in 100 µL DMSO, and absorbance

measured at 570 nm. Cell viability was calculated as:

Cell Viability (%) = (Absorbance_treated / Absorbance_control) × 100

IC_{50} values were determined by non-linear regression analysis using GraphPad Prism software.

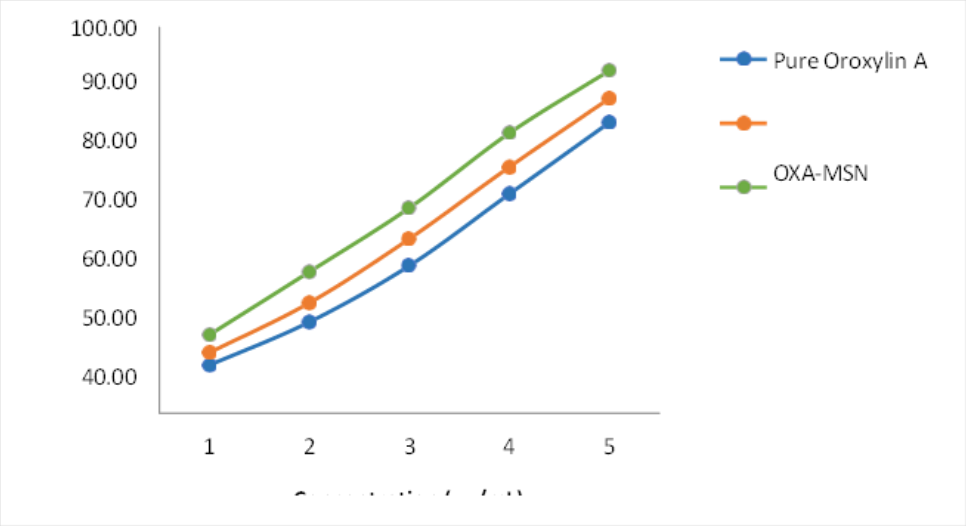

Fig 3:Concentration-dependent cytotoxicity (%)

9.7.2 Concentration-Dependent Cytotoxicity

Pure Oroxylin A exhibited IC_{50} of 38.24 ± 1.46 µg/mL. Unfunctionalized OXA-MSN demonstrated inhanced cytotoxicity with IC_{50} of 26.18 ± 1.22 µg/mL, reflecting improved drug delivery via mesoporous silica carrier. The zwitterionic-functionalized OXA-SB12-MSN-DC exhibited highest cytotoxic potency with IC_{50} of 17.86 ± 0.94 µg/mL, representing a 2.14-fold improvement over pure Oroxylin A.

9.7.3 Comparative IC_{50} Analysis

Table 11 : Comparative IC_{50} Analysis

Sample	IC_{50} (µg/mL)	Fold Reduction vs. Pure Drug
Pure Oroxylin A	38.24 ± 1.46	1.00
OXA-MSN (unfunctionalized)	26.18 ± 1.22	1.46
OXA-SB12-MSN-DC (zwitterionic)	17.86 ± 0.94	2.14

At 80 µg/mL concentration:

- Pure Oroxylin A: 75.4 ± 3.38% cytotoxicity, 24.6 ± 3.38% viability
- OXA-MSN: 81.6 ± 3.12% cytotoxicity, 18.4 ± 3.12% viability
- OXA-SB12-MSN-DC: 88.8 ± 2.84% cytotoxicity, 11.2 ± 2.84% viability

9.7.4 Mechanistic Interpretation

The superior cytotoxicity of OXA-SB12-MSN-DC arises from synergistic contributions:

1. **Improved drug solubilization:** Mesopore incorporation transforms crystalline Oroxylin A into amorphous form with enhanced dissolution kinetics, increasing bioavailable drug concentration at the cell surface.
2. **Enhanced cellular internalization:** Zwitterionic dipole moment (~25 Debye for SB12) facilitates electrostatic interactions with negatively charged cancer cell membranes

(cancer cells have higher negative surface charge than normal cells due to elevated anionic phospholipid content like phosphatidylserine). This drives increased receptor-independent endocytosis but with greater cellular uptake rate than passive diffusion.

3. **Sustained intracellular drug release:** After endolysosomal trafficking, siloxane and amide bonds may be partially cleaved by acidic endolysosomal pH (5.0–5.5) and lysosomal enzymes, releasing free Oroxylin A over extended periods and maintaining intracellular concentrations above apoptotic thresholds.

4. **Apoptosis pathway engagement:** Oroxylin A mechanisms (PI3K/AKT/mTOR suppression, NF-κB inhibition, G2/M arrest, Bcl-2 family modulation, p53 activation) collectively activate caspase cascade. Phase contrast microscopy confirmed extensive apoptosis-specific morphological changes (membrane blebbing, apoptotic body formation, cell detachment).

9.7.5 Phase Contrast Microscopy Analysis

Microscopic examination at 48 h post-treatment revealed:

- **Untreated control:** Intact confluent monolayer, polygonal cell morphology, prominent nuclei, organized cytoskeleton.
- **Pure Oroxylin A treatment:** Moderate cell density reduction, limited morphological alterations, some cell rounding.
- **OXA-MSN treatment:** Notable cell loss, more pronounced cell rounding and detachment.
- **OXA-SB12-MSN-DC treatment:** Maximum disruption—extensive cell rounding, membrane blebbing, apoptotic body formation (indicated by arrows in micrographs), significant cell detachment—characteristic features of caspase-mediated apoptosis.

These morphological changes collectively suggest caspase-3 activation, DNA fragmentation, and apoptotic body formation at 48 h post-treatment with zwitterionic-functionalized nanoparticles.

10.CONCLUSION

Lung cancer continues to represent one of the greatest challenges in modern oncology owing to its high mortality rate, molecular heterogeneity, late-stage diagnosis, and the development of resistance to conventional therapeutic modalities. Although advances in targeted therapy and immunotherapy have improved clinical outcomes in selected patient populations, significant limitations related to systemic toxicity, poor tumor selectivity, multidrug resistance, and unfavorable pharmacokinetic profiles remain major barriers to effective treatment.

Nanotechnology-based drug delivery systems have emerged as promising strategies to overcome these challenges by improving drug solubility, biodistribution, tumor accumulation, and controlled release characteristics. Among the available nanocarriers, mesoporous silica nanoparticles have attracted considerable attention due to their large surface area, tunable pore structure, high drug-loading capacity, excellent biocompatibility, and versatile surface functionalization capabilities. Furthermore, zwitterionic surface engineering has provided an effective alternative to conventional stealth technologies by minimizing protein corona formation, reducing macrophage-mediated clearance, prolonging systemic circulation, and

enhancing tumor accumulation through the enhanced permeability and retention effect.

Oroxylin A is a naturally occurring flavonoid with significant anticancer potential mediated through modulation of multiple oncogenic pathways, including PI3K/AKT/mTOR, NF-κB, apoptosis-related signaling, and tumor metabolic pathways. However, its poor aqueous solubility, rapid metabolism, short biological half-life, and limited bioavailability substantially restrict its clinical translation. The integration of Oroxylin A with zwitterionic functionalized mesoporous silica nanoparticles offers a rational and multifunctional therapeutic platform capable of addressing these limitations through improved drug protection, enhanced intracellular delivery, prolonged circulation, and sustained release behavior.

Collectively, the convergence of mesoporous silica nanotechnology, zwitterionic surface modification, and natural-product-based therapeutics represents a promising strategy for next-generation lung cancer treatment. Continued research focusing on large-scale manufacturing, long-term safety evaluation, regulatory considerations, and clinical translation will be essential to realize the full potential of these advanced nanomedicine platforms in precision oncology and personalized cancer therapy..

REFERENCES

1. Bray F, Laversanne M, Sung H, Ferlay J, Siegel RL, Soerjomataram I, et al. Global cancer statistics 2022: GLOBOCAN estimates of incidence and mortality worldwide for 36 cancers in 185 countries. CA Cancer J Clin. 2024;74(3):229–263. doi:10.3322/caac.21834
2. Mathur P, Sathishkumar K, Chaturvedi M, Das P, Sudarshan KL, Santhappan S, et al. A clinicoepidemiological profile of lung cancers in India: Results from the National Cancer Registry Programme. Indian J Med Res. 2022;156(1):168–177. doi:10.4103/0971-5916.362038
3. Kanodra NM, Bhatt SP, Bhattacharya S, Srivastava PK, Murali MR, Bhardwaj A. Lung cancer screening in India: Preparing for the future using smart tools and biomarkers to identify highest risk individuals. Indian J Med Res. 2025;161(1):8–19. doi:10.25259/IJMR_481_2024
4. Alduais Y, Zhang H, Fan F, Chen J, Chen B. Non-small cell lung cancer (NSCLC): A review of risk factors, diagnosis, and treatment. Medicine (Baltimore). 2023;102(8):e32899. doi:10.1097/MD.0000000000032899
5. Ombrato L, Gkountela S, Bivona TG, Montagner M. Small cell lung cancer — tumor biology and heterogeneity. Cancers (Basel). 2024;16(4):753. doi:10.3390/cancers16040753
6. Guo J, Zhang W, Zhao K, Liu L, Xu W, Zhao W. Prognostic impact of KRAS-TP53 co-mutations in patients with early-stage non-small cell lung cancer: a single-center retrospective study. Int J Mol Sci. 2025;26(13):5987. doi:10.3390/ijms26135987
7. Gu W, Liu D, Tang Z, Lai Q, Wang X, Zhang H, et al. The prognosis of TP53 and its concomitant EGFR mutation in patients with advanced lung adenocarcinoma with intracranial metastasis treated with EGFR-TKIs. Front Oncol. 2024;13:1288468. doi:10.3389/fonc.2023.1288468
8. Chen K, Luo L, Li Y, Yang G. Reprogramming the immune microenvironment in lung cancer. Front Immunol. 2025;16:1684889. doi:10.3389/fimmu.2025.1684889
9. Huang Z, Xie T, Xie W, Chen Z, Wen Z, Yang L. Research trends in lung cancer and the tumor microenvironment: a bibliometric analysis of studies published from 2014 to 2023. Front Oncol. 2024;14:1428018. doi:10.3389/fonc.2024.1428018
10. Xie L, Xiao D, Deng Z, Su X, Lin X, Cai F, et al. A novel therapeutic outlook:

Classification, applications and challenges of inhalable micron/nanoparticle drug delivery systems in lung cancer. Int J Oncol. 2024;64(4):38. doi:10.3892/ijo.2024.5626
11. Pasello G, Pavan A, Attili I, Guarneri V, Conte P. Cutting-edge therapies for lung cancer. Int J Mol Sci. 2024;25(5):2880. doi:10.3390/ijms25052880
12. Chen Y, Shan X, Li Y, Zhang Y, Wang B, Duan M, et al. Research trends and highlights in PD-1/PD-L1 inhibitor immunotherapy in lung cancer: a bibliometric analysis. Front Immunol. 2025;16:1569487. doi:10.3389/fimmu.2025.1569487
13. Ganesan M, Narayanan NK, Basalingappa KM, Pragasam SJ, Pathak S, Banerjee A. Emerging therapeutic strategies to overcome drug resistance in cancer cells. Cancers (Basel). 2024;16(14):2488. doi:10.3390/cancers16142488
14. Pasquale Marrazzo, Carmen Caserta, Claudia Ferrante, Luca Chiereghin, Manuela Ventura. Engineered nanocarriers for targeted lung cancer therapy: mechanistic innovations and recent clinical progress. Int J Nanomedicine. 2025;20:8097–8131. doi:10.2147/IJN.S527006
15. Agrawal U, Sharma R, Gupta M, Vyas SP. Is nanotechnology a boon for oral drug delivery? Drug Discov Today. 2014;19(10):1530–1546. doi:10.1016/j.drudis.2014.04.011
16. Tenchov R, Bird R, Curtze AE, Zhou Q. Lipid nanoparticles — from liposomes to mRNA vaccine delivery, a landscape of research diversity and advancement. ACS Nano. 2021;15(11):16982–17015. doi:10.1021/acsnano.1c04996
17. Yadav D, Sharma PK, Singh K, Koul V. Advances in nanoparticle-based targeted drug delivery systems for colorectal cancer therapy: a review. Pharmaceutics. 2023;15(7):1815. doi:10.3390/pharmaceutics15071815
18. Attia MF, Anton N, Wallyn J, Omran Z, Vandamme TF. An overview of active and passive targeting strategies to improve the nanocarriers efficiency to tumour sites. J Pharm Pharmacol. 2019;71(8):1185–1198. doi:10.1111/jphp.13098
19. Waheed I, Ali A, Tabassum H, Khatoon N, Zhou X, Pei R. Nanoparticle-based drug delivery systems for cancer treatment: a comprehensive review. RSC Adv. 2024;14(13):8690–8702. doi:10.1039/d3ra08831c
20. Greish K, Mathur A, Bakhiet M, Taurin S. Nanomedicine: perspectives on improving the EPR effect for tumor targeting. J Cancer Res Clin Oncol. 2023;149(8):4349–4366. doi:10.1007/s00432-023-04651-3
21. Bhattarai N, Bhattarai M, Bhatta S, Bhuwal AK, Gyawali L, Pathak L, et al. Advances in nanoparticle-mediated cancer therapeutics: current research and future perspectives. Cancer Pathog Ther. 2025;3(1):1–17. doi:10.1016/j.cpt.2024.11.002
22. Danhier F. To exploit the tumor microenvironment: since the EPR effect fails in the clinic, what is the future of nanomedicine? J Control Release. 2016;244(Pt A):108–121. doi:10.1016/j.jconrel.2016.11.015
23. Kang H, Rho S, Stiles WR, Hu S, Baek Y, Hwang DW, et al. Size-dependent EPR effect of polymeric nanoparticles on tumor targeting. Adv Healthc Mater. 2020;9(1):e1901223. doi:10.1002/adhm.201901223
24. Alkilany AM, Elhissi A, Alshaer W, Kunwar A, Giri J. Editorial: Anti-cancer drug delivery: lipid-based nanoparticles. Front Oncol. 2023;13:1248272. doi:10.3389/fonc.2023.1248272
25. Fernandes DA. Review on metal-based theranostic nanoparticles for cancer therapy and imaging. ACS Appl Bio Mater. 2023;6(9):3836–3863. doi:10.1177/15330338231191493
26. Lazarovits J, Chen YY, Sykes EA, Chan WCW. Nanoparticle-blood interactions: the implications on solid tumour targeting. Chem Commun (Camb). 2015;51(14):2756–2767. doi:10.1039/c4cc07644c

27. Bhatt DL, Mehta C. Adaptive designs for clinical trials. N Engl J Med. 2016;375(1):65–74. doi:10.1056/NEJMra1510061

HOW TO CITE: Mehetre Rutuja, Dr. Sachin Aglave, Dr. Vijay Jadhav, Dr. Nitin Jain, Dr. Usha Jain, Oroxylin A-Loaded Zwitterionic Mesoporous Silica Nanoparticles: A Promising Platform for Targeted Lung Cancer Therapy, Int. J. of Pharm. Sci., 2026, Vol 4, Issue 7, 507-535. https://doi.org/10.5281/zenodo.21154768